Nano Research

Open Access

Research Article

Star-concave iron-metal-organic frameworks with enhanced light trapping for boosting synergistic adsorption-photoreduction of the dominant chromium species

Yingrun Cai[1,§], Yuqing Gao[1,§], Ying Pan[2,§], Jianqiang Liu[2] ✉, Ke Feng[1], Chenggan Pei[3], Abhinav Kumar[4] ✉, Yujun Zhu[5], Huan Pang[3] ✉, and Fei Ke[1] ✉

[1] *Department of Applied Chemistry, Agricultural Photocatalysis Laboratory, School of Materials and Chemistry and National Key Laboratory for Tea Plant Germplasm Innovation and Resource Utilization, Anhui Agricultural University, Hefei 230036, China*
[2] *Guangdong Medical University Key Laboratory of Research and Development of New Medical Materials, School of Pharmacy, Guangdong Medical University, Dongguan 523808, China*
[3] *School of Chemistry and Chemical Engineering, Yangzhou University, Yangzhou 225009, China*
[4] *Department of Chemistry, Faculty of Science, University of Lucknow, Lucknow 226007, India*
[5] *Department of Pharmacy and Biomedical Engineering, Clinical College of Anhui Medical University, Hefei 230031, China*
[§] *Yingrun Cai, Yuqing Gao, and Ying Pan contributed equally to this work.*

Cite this article: *Nano Research*, **2026**, *19*, 94908052. https://doi.org/10.26599/NR.2025.94908052

ABSTRACT: Creating a specific shape with hierarchically porous structure of metal-organic frameworks represents an effective strategy to enhance the adsorption and photocatalytic performance yet remains rather challenging. Herein, we present a facile linker competitive coordination induced interface assembly strategy to synthesize a series of star-concave metal-organic frameworks (MOFs) (Fe-MIL-101) with rich hierarchical pores. This strategy of star-concave Fe-MIL-101 depends on the electronegativity difference of the two linkers to produce an *in-situ* oriented growth with controllable kinetics nucleation and structural evolution. As a result, the optimized star-concave Fe-MIL-101-2 with multiple physical-chemical effects endows enhanced visible-light trapping, preferred charge separation, and optimized the local electronic structure. In comparison with the slightly concave Fe-MIL-101 and solid octahedron Fe-MIL-101-NH_2, the star-concave Fe-MIL-101-2 displays a clear superiority in the adsorption-photoreduction of Cr(VI) under visible-light irradiation. Furthermore, the X-ray absorption fine structure spectroscopy, finite element method, and density functional theory calculations are performed to reveal the local electronic structure of star-concave Fe-MIL-101-2, understanding the mechanisms behind the boosting synergistic adsorption-photoreduction of Cr(VI) removal performance. This work provides a new perspective for the rational construction of MOFs-based photocatalysts with high activity for Cr(VI) removal through shape engineering.

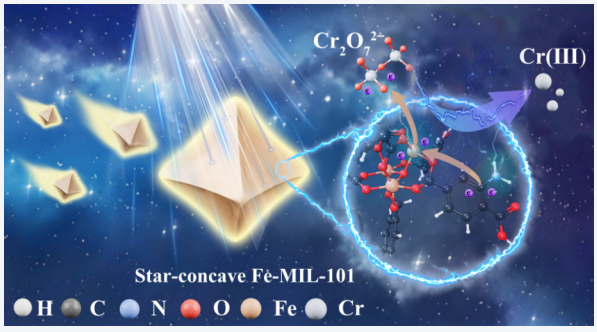

KEYWORDS: metal-organic frameworks, star-concave structure, enhanced light trapping, photocatalysis, Cr(VI) reduction

1 Introduction

Safeguarding the human environment from water pollution is a major concern because of the rapid pace of modernization [1]. Heavy metal ions, especially hexavalent chromium ions (Cr(VI)) are regarded as environmentally non-biodegradable and can cause serious diseases including kidney failure, genetic defects, and cancers [2]. Owing to the great threat to the environment and human health, the World Health Organization has set the concentration line of Cr(VI) at 50 ppb in drinking water [3]. Thus, developing an efficient technology to eliminate Cr(VI) at the ppb level from wastewater is an urgent demand. To address this issue, various methods including adsorption, membrane separation, ion exchange, and photocatalytic reduction have been widely employed for the removal of Cr(VI) [4]. Among them, photocatalytic

Received: July 23, 2025; **Revised:** September 3, 2025
Accepted: September 8, 2025

✉Address correspondence to Jianqiang Liu, jianqiangliu8@gdmu.edu.cn; Abhinav Kumar, abhinavmarshal@gmail.com; Huan Pang, panghuan@yzu.edu.cn; Fei Ke, kefei@ahau.edu.cn

reduction can be regarded as the most effective remediation method to reduce Cr(VI) to less toxic Cr(III) owing to its low cost, environmental friendliness, and energy saving [5]. Compared to the high toxicity of Cr(VI), photoreduction product of Cr(III) is less toxic with easy precipitation from water for further applications. In this case, various photocatalysts have been developed for the photoreduction of Cr(VI), including $Co_3O_{4\text{-}Ov}/TiO_2$ [6], Sn-BOC/CQDs [7], Co_3O_4/g-C_3N_4 [8], and PAN/TiO_2/PANI [9]. However, most traditional photocatalysts remain far from satisfactory due to insufficient active sites, poor adsorption, and low visible-light energy utilization [10]. Therefore, the development of highly efficient photocatalysts with outstanding adsorption and photoreduction synergy effect remains a significant challenge.

Metal-organic frameworks (MOFs) as an important class of porous materials have sparked widespread research attention in adsorption and photocatalysis applications [11–13]. This is due to their large surface area, abundant functional sites, diverse crystalline architectures and tunable bandgap structure which are ideal requirements for environmental remediation [14]. Thus, numerous MOFs have been designed for adsorption and photoreduction of Cr(VI) under visible light [15]. However, their intrinsic low separation efficiency of photoexcited electron-hole pairs profoundly restricts the photocatalytic activity [16]. Generally, the design of MOFs-based heterostructure has been suggested to obtain the synergistic effect of components, resulting in enhanced separation efficiency of electron-hole pairs [17]. In practice, enormous MOFs-based heterostructures (e.g., MIL-101(Fe)/BiOBr [18], UiO-66-NH_2@HDU-25 [19], MIL-101(Fe)/Bi_2WO_6 [20], Fe_3O_4@Fe-TPPE [21]) have been fabricated for highly enhanced photoreduction activity of Cr(VI) from water. Nevertheless, this heterostructure strategy usually results in blockage of the pores, narrow micropore size distribution, and complicated procedure conditions.

On the other hand, a promising strategy based on shape-dependent physical and chemical performance has been developed for synthesizing MOFs nanostructures for widespread superior applications [22]. MOFs shape can be well controlled through modifying the solvents, surfactants, reaction time or coordination environment of metal and organic ligands. In this case, plenty of bottom-up based strategies have been reported for excellent control on the shape of MOFs nanostructures [23]. Among the various morphology of MOFs (e.g., hollow, spindle, solid octahedron, nanorod), the concave shapes display low coordinated atoms over the surface and highly accessible outer and interior region, which endows them more active sites [24–26]. Meanwhile, the high index facets, stability and practical applicability of concave shape enable it the preferred photocatalytic active sites. Particularly, the highly enhanced light-matter interaction in the concave shape structure makes them vast opportunities in photocatalysis [27]. For instance, Yu et al. reported a soft interface adaptive transformation method to generate octahedral NH_2-MIL-125-derived concave TiO_2 nanoparticles to enhance the photocatalytic degradation activity of methylene blue [28]. Recently, a series of spiral-concave Prussian Blue based MOFs with rich active sites were synthesized by Pang et al. through a novel oriented adsorption-ion exchange method for high oxygen evolution reactions [29]. Despite these pioneering works, the construction of concave MOFs with rich hierarchical pores in exquisite control remains a great challenge.

Herein, we present an ingenious linker competitive coordination induced interface assembly strategy to synthesize star-concave iron-metal-organic frameworks (Fe-MIL-101) with highly controllable kinetics nucleation and rich hierarchical pores. Fe-MIL-101 has a highly water stable performance with hexacoordinated Fe_3O clusters connected by H_2BDC organic linkers [$Fe_3(\mu_3\text{-}O)Cl(H_2O)_2(BDC)_3$]. It has two quasi-spherical cages of 2.9 and 3.4 nm. This strategy hinges on the different ligands electronegativities of 2-aminoterephthalic acid ($H_2BDC\text{-}NH_2$) and terephthalic acid (H_2BDC) to produce an *in-situ* oriented competitive coordination nucleation. Additionally, various Fe-MIL-101 architectures, including spindle, solid octahedron, slightly concave octahedron, star-concave octahedron can be modulated by controlling the growth kinetics and molar ratio of the two linkers. Finite element method (FEM) and density functional theory (DFT) calculations and experimental characterizations exhibit enhanced visible-light harvesting and optimize the local electronic structure of the star-concave facets in the Fe-MIL-101, thereby enhancing adsorption and photoreduction performance for the Cr(VI) remove. This novel *in-situ* oriented competitive coordination assembly strategy paves new insights into the synthesis of MOF-based distinctive shape-dependent photocatalysts.

2 Results and discussion

The star-concave Fe-MIL-101 nanoparticles are synthesized through an *in-situ* oriented competitive coordination assembly of the MOFs precursors $H_2BDC\text{-}NH_2$, H_2BDC, $FeCl_3{\cdot}6H_2O$ in dimethylformamide (DMF) solution (Fig. 1(a)). The as-prepared Fe-MIL-101 nanoparticles with mixed linkers are denoted as Fe-MIL-101-*x*, where *x* represents the molar ratio of H_2BDC to $H_2BDC\text{-}NH_2$. The structure and morphology of the star-concave Fe-MIL-101 were first characterized by scanning electron microscopy (SEM). Figure 1(b) shows the pure Fe-MIL-101 is a slightly concave octahedron with diameter of 500 nm (Figs. 1(b) and 1(e)), while the obtained Fe-MIL-101-NH_2 shows a solid octahedron with smooth surface and particle size of 400 nm (Figs. 1(c) and 1(f)). Significantly, the as-synthesized Fe-MIL-101-2 exhibits a distinct star-concave morphology evolution with particle size of 600 nm (Figs. 1(d) and 1(g)), demonstrating an inward contraction during the competitive coordination assembly process. From the corresponding energy-dispersive spectroscopy (EDS) elemental mapping revealed that Fe, C, N, and O elements are homogeneously distributed in the star-concave Fe-MIL-101-2 frameworks (Fig. 1(k)). The structural characterization is further performed by transmission electron microscopy (TEM). TEM images of the Fe-MIL-101-2 show relatively low contrast and bright spots in the interior part as compared to those of the Fe-MIL-101 and Fe-MIL-101-NH_2, suggesting the star-concave structure with rich mesopores of Fe-MIL-101-2 (Figs. 1(h)–1(j)).

Powder X-ray diffraction (PXRD) patterns show that the sharp and strong diffraction peaks of star-concave Fe-MIL-101-2 match well with those of Fe-MIL-101 and Fe-MIL-101-NH_2, indicating that all the samples have the same MIL-101-based framework crystalline architecture (Fig. 1(l)) [30]. The thermogravimetric analysis (TGA) (Fig. S1 in the Electronic Supplementary Material (ESM)) and Fourier-transform infrared (FTIR) spectrum (Fig. S2 in the ESM) of star-concave Fe-MIL-101-2 were similar with the solid octahedron Fe-MIL-101-NH_2. Moreover, the porous feature of the samples was analyzed by nitrogen adsorption–desorption isotherms. Figure 1(m) shows that all the three Fe-MIL-101 samples display type-IV isotherms. Especially, distinct from Fe-MIL-101 and Fe-MIL-101-NH_2, the large hysteresis loop in star-concave Fe-

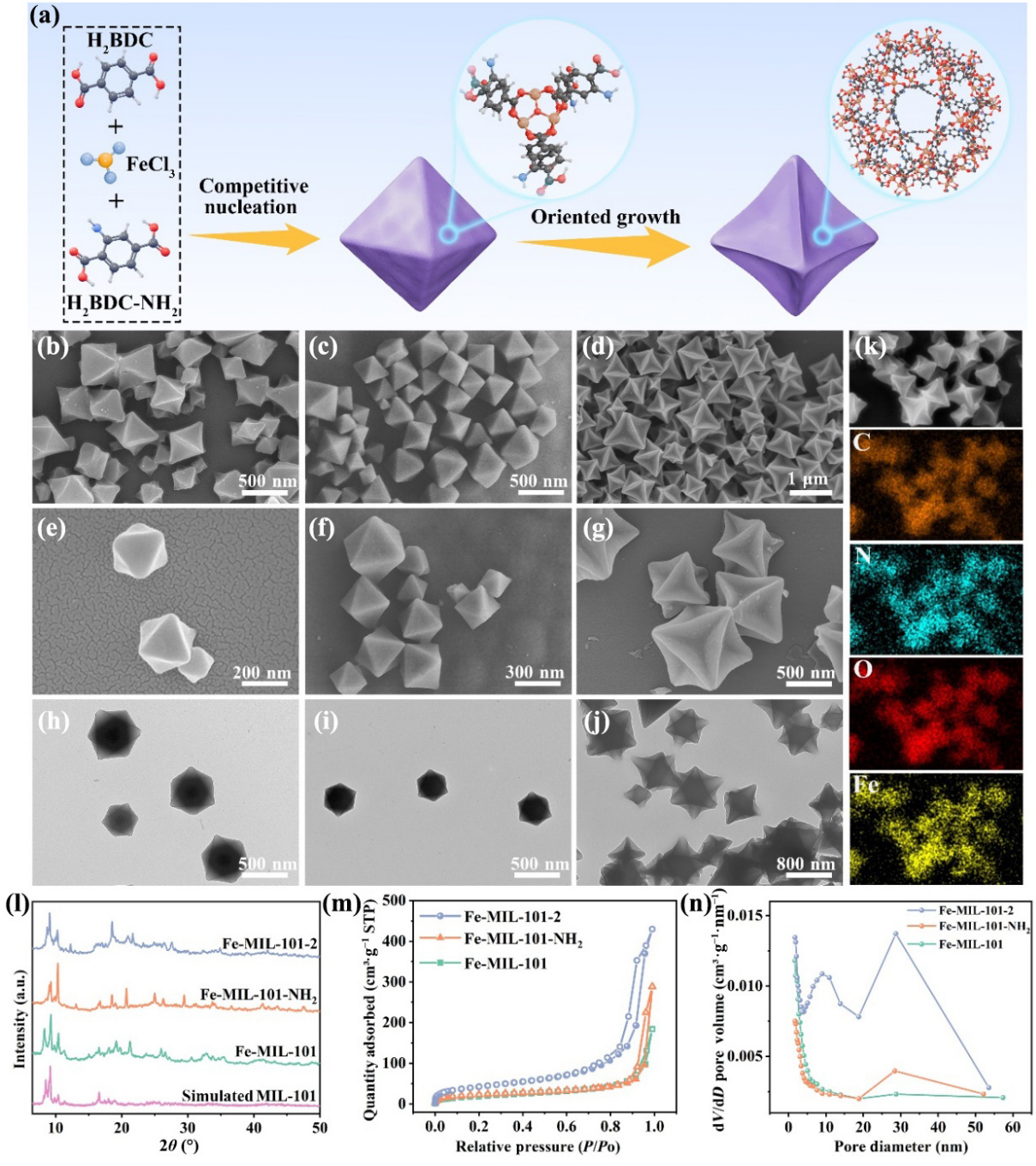

Figure 1 (a) Schematic representation of the formation of star-concave Fe-MIL-101. SEM and TEM images of Fe-MIL-101 ((b), (e), and (h)), Fe-MIL-101-NH_2 ((c), (f), and (i)), Fe-MIL-101-2 ((d), (g), and (j)), and the corresponding elemental mappings for C, N, O, and Fe elements of Fe-MIL-101-2 (k), PXRD patterns (l), nitrogen adsorption–desorption isotherms (m), and BJH pore size distributions (n) for Fe-MIL-101, Fe-MIL-101-NH_2 and Fe-MIL-101-2.

MIL-101-2 indicates the existence of large mesopores. The Brunauer–Emmett–Teller (BET) specific surface areas of Fe-MIL-101, Fe-MIL-101-NH_2, and Fe-MIL-101-2 are measured at 85.40, 80.60, and 163.67 $m^2 \cdot g^{-1}$, respectively (Table S1 in the ESM). As expected, much more pore-size distribution of star-concave Fe-MIL-101-2 falls in the mesopore region (9.0, 28.7 nm) according to the Barrett–Joyner–Halenda (BJH) model (Fig. 1(n)). The higher BET specific surface area and pore-size of Fe-MIL-101-2 than Fe-MIL-101, Fe-MIL-101-NH_2 can be ascribed to the special star-concave structure and cooperative assembly of the two linkers.

Meanwhile, the enhanced light trapping of star-concave Fe-MIL-101-2 was conducted by FEM. The electromagnetic (EM) field enhancement of three different morphologies is depicted in Fig. 2(a). According to the simulation, the values of surface electric field enhancement of solid octahedron, slightly concave octahedron and star-concave octahedron are 4.94, 5.86, and 13.7, respectively. The surface electric field enhancement value increases obviously with the increase in the concave degree of the nanoparticles. This phenomenon suggested that the concave sharp is crucial for enhancing the light trapping. Subsequently, the electric field enhancement of the two dimensional (2D) shows that the star-concave Fe-MIL-101-2 has the largest value of 40.1 (Fig. 2(b))

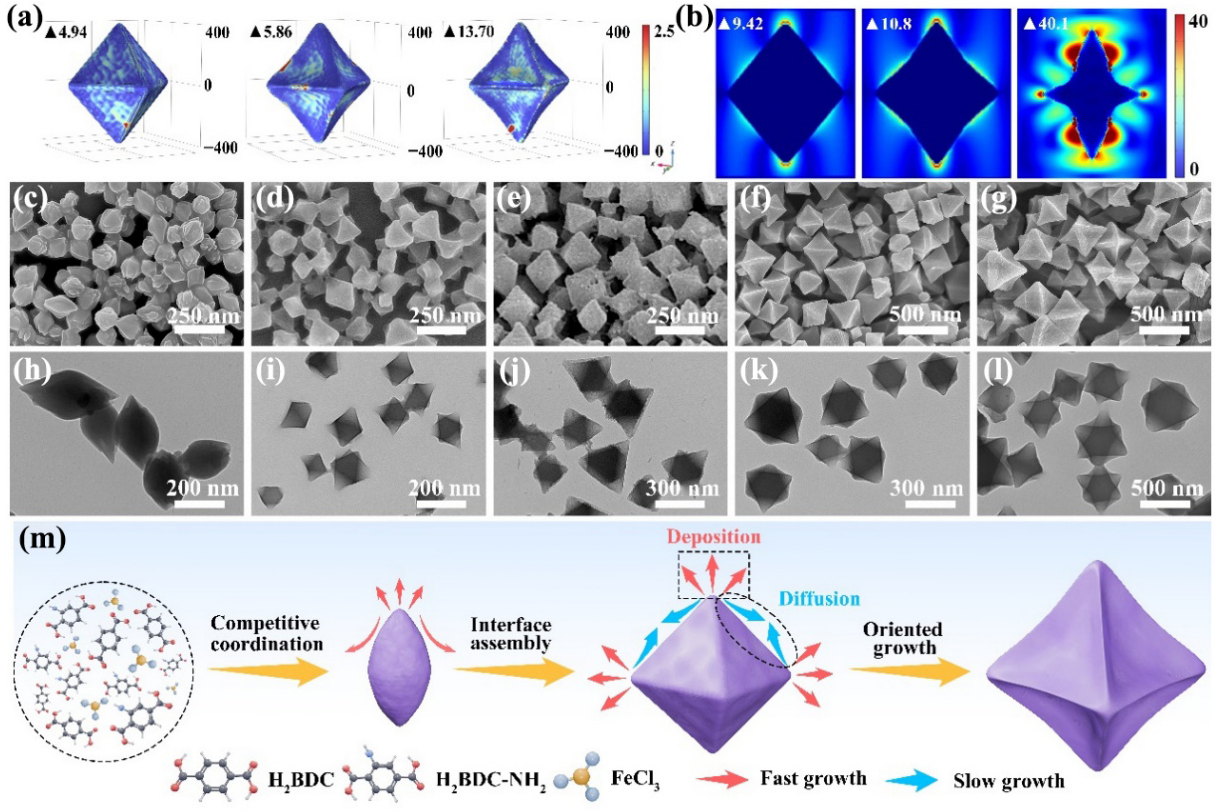

Figure 2 Contour plots of electric field amplitudes three dimensional (a) and two dimensional (b) cross sections for solid octahedron, slightly concave octahedron and star-concave morphology with the finite element method. SEM and TEM images of the Fe-MIL-101-2 prepared with different reaction times: 2 h ((c) and (h)), 5 h ((d) and (i)), 10 h ((e) and (j)), 15 h ((f) and (k)), and 18 h ((g) and (l)). Formation mechanism of star-concave Fe-MIL-101-2 (m).

which is 4.3 and 3.7 times that of solid octahedron (9.42) and slightly concave octahedron (10.8). These results indicate that the star-concave structure of Fe-MIL-101-2 can supply larger absorption cross section, which is beneficial to light focusing and transfer photon energy.

The structural evolution of star-concave Fe-MIL-101-2 depends on the competition between the deposition and diffusion rates of the mixed linkers system during the growth process. To better understand the formation pathway of the star-concave structure, the morphologies of Fe-MIL-101 (Fig. S4 in the ESM), Fe-MIL-101-NH_2 (Fig. S5 in the ESM), and Fe-MIL-101-2 (Fig. 2) obtained at different reaction time intervals were performed. From observation in Figs. 2(c) and 2(h), the spindle nanostructure with diameter of 100 nm can be seen at the initial stage of 2 h. As the reaction time reaches 5 h, the crystals of Fe-MIL-101-2 transfer to solid octahedron morphology with diameter of 150 nm (Figs. 2(d) and 2(i)). With the increase in time to 10 h, the framework crystals transfer to more uniform solid octahedron morphology with rough surfaces and the particle size increases rapidly to 250 nm (Figs. 2(e) and 2(j)). Notably, when the reaction time increases to 15 h, the products exhibited an obvious concave nanostructure with particle size of 400 nm (Figs. 2(f) and 2(k)). As the time is further extended to 18 h, a perfect star-concave octahedron nanostructure with particle size of 600 nm is detected for the Fe-MIL-101-2 (Figs. 2(g) and 2(l)). The structural evolution of Fe-MIL-101-2 was also monitored using PXRD (Fig. S6 in the ESM) and nitrogen adsorption–desorption isotherms (Fig. S7 in the ESM).

Based on the above results, we propose a possible mechanism of the structural formation of the star-concave octahedron Fe-MIL-101-2. Figure 2(m) shows the schematic illustration for the evolution of Fe-MIL-101-2 with different morphologies. At the initial stage, the lower electronegativity of H_2BDC-NH_2 can coordinate with Fe^{3+} first and then other part of H_2BDC is induced to reaction with the coordination unsaturated Fe^{3+} active center to form the secondary building units [31], resulting in typical spindle-shaped particles to be formed. During the competitive coordination nucleation process of the two linkers and Fe^{3+}, the edges and surfaces energy is much lower than that of corners, thus the framework building units preferentially deposit at the corner [25]. Over time, the building units can move to the surfaces or edges through diffusion and with extended reaction time resulting in the creation of solid octahedron-shaped MOFs. While the reaction further proceeds, the particle size of the frameworks gradually increases which leads to the decreased surface diffusion kinetics. Consequently, the edges and surfaces increase slowly, generating a uniform star-concave octahedron structure of Fe-MIL-101-2.

According to the above proposed mechanism, the variation in morphology of Fe-MIL-101 through the control of the molar ratio of H_2BDC and H_2BDC-NH_2 was performed. As shown in Figs. S15 and S16 in the ESM, the competitive coordination between different molar ratio of H_2BDC and H_2BDC-NH_2 to Fe^{3+} center can obviously influence the *in-situ* oriented nucleation and further influence the morphology of Fe-MIL-101. As seen, when the molar ratio of H_2BDC/H_2BDC-NH_2 is 0.25 and 0.5, the product of Fe-MIL-101-0.25 and Fe-MIL-101-0.5 particles exhibited a slightly concave structure (Figs. S15(a), S15(b), S16(a), and S16(b) in the ESM). This could be due to the high growth speed of the Fe-MIL-101 with the high concentration of H_2BDC-NH_2 during the

reaction. With the molar ratio of $H_2BDC/H_2BDC\text{-}NH_2$ increased to 1 and 2, the products of Fe-MIL-101-1 and Fe-MIL-101-2 showed an obvious concave structure (Figs. 1(d), 1(g), 1(j), and Fig. S15(c) in the ESM). However, when the molar ratio of $H_2BDC/H_2BDC\text{-}NH_2$ continuously increased to 4, the product of Fe-MIL-101-4 particles exhibited a slightly concave structure again, as shown in Figs. S15(d) and S16(d) in the ESM. These results clearly indicate that the introduction of an appropriate molar ratio of $H_2BDC/H_2BDC\text{-}NH_2$ during the synthesis of Fe-MIL-101 is important to obtain a uniform star-concave morphology. Correspondingly, the real content ratios of H_2BDC and $H_2BDC\text{-}NH_2$ in the Fe-MIL-101-*x* were measured by Ultra Performance Liquid Chromatography-Mass Spectrometry (UPLC-MS) (Table S5 in the ESM). The PXRD patterns exhibited that all the Fe-MIL-101-*x* structures have the characteristic peaks of MIL-101 (Fig. S17 in the ESM) and the BET surface areas and the porous feature are shown in Figs. S18 and S19 in the ESM.

Inspired by the star-concave nanostructure unique merits of Fe-MIL-101-2, adsorption and photocatalytic reduction of Cr(VI) was performed to study the photocatalytic activity. As shown in Fig. 3(a), the adsorption initially proceeded by immersing different Fe-MIL-101 in Cr(VI) solution (10 ppm) versus the time without light. We can see that all the mixed linkers of Fe-MIL-101-*x* have a higher adsorption capacity than the single linker of Fe-MIL-101. The removal efficiency increases with increasing $H_2BDC/H_2BDC\text{-}NH_2$ molar ratio up to 2 and then decreases. For single Fe-MIL-101 (42%) and Fe-MIL-101-NH_2 (48%), relatively low removal efficiencies are observed while Fe-MIL-101-2 has the optimal adsorption performance of 57% within 120 min. These results indicate that the mixed linkers of H_2BDC and $H_2BDC\text{-}NH_2$ provide a necessary synergistic effect for the remove of Cr(VI). The time-dependent Cr(VI) removal data were fitted by the pseudo-second-order kinetic modal (Fig. S22 in the ESM). The corresponding adsorption rate constant (k_2) value of Fe-MIL-101-2 was 0.078 $g \cdot mg^{-1} \cdot min^{-1}$, which is 3.4 and 2.4 times higher than Fe-MIL-101 (0.023 $g \cdot mg^{-1} \cdot min^{-1}$) and Fe-MIL-101-$NH_2$ (0.032 $g \cdot mg^{-1} \cdot min^{-1}$)

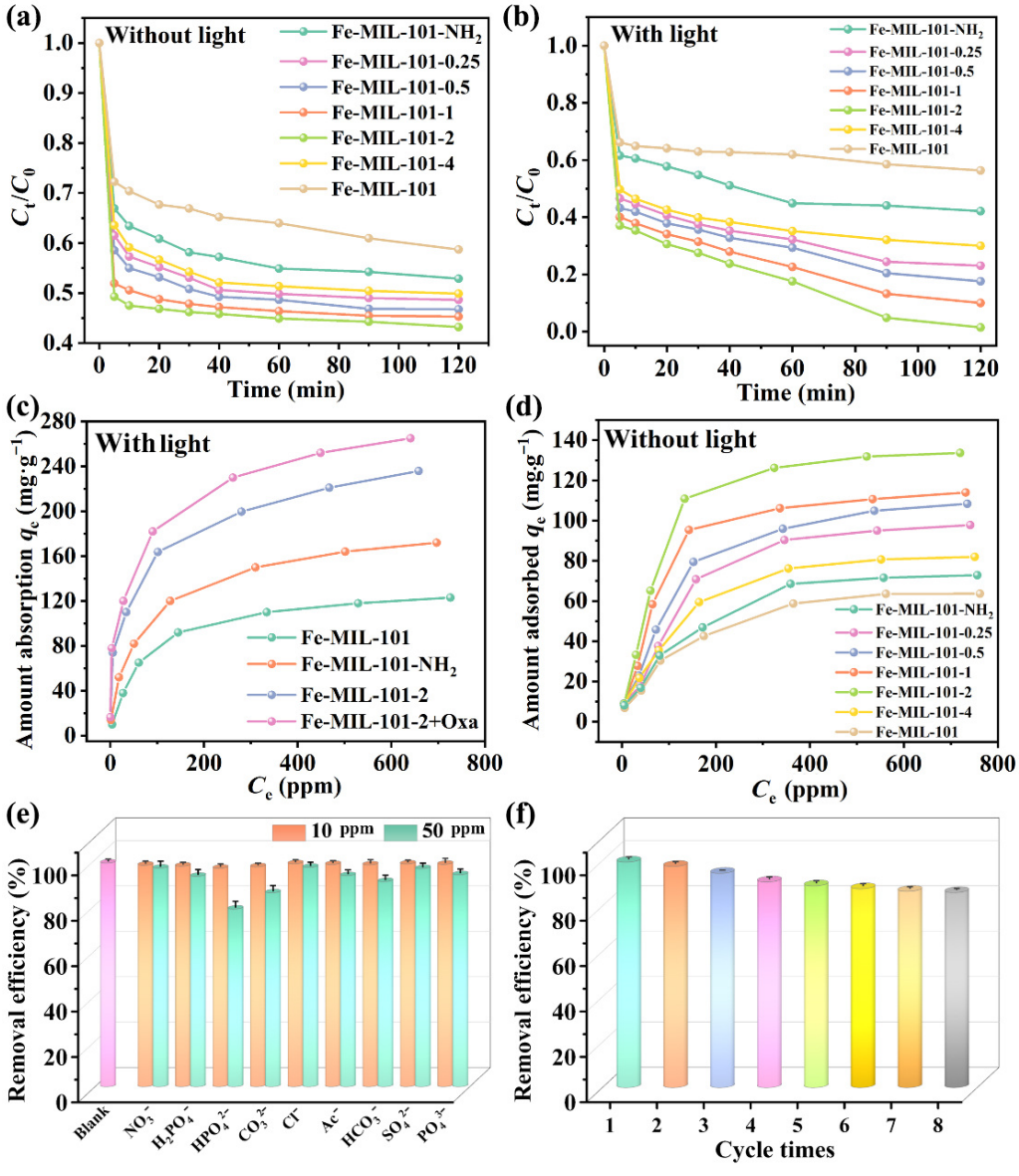

Figure 3 Adsorption kinetics behavior of different Fe-MIL-101 samples toward Cr(VI) without (a) and with (b) light. The isotherms of Cr(VI) uptake by different Fe-MIL-101 samples with (c) and without (d) light. Influence of competitive anions (e) and regenerated (f) on Cr(VI) removal over Fe-MIL-101-2.

demonstrating outstanding adsorption kinetics (Table S6 in the ESM). Significantly, whereas in the presence of visible-light irradiation, all of the different Fe-MIL-101 samples exhibit smoothly enhanced Cr(VI) uptake performance as compared with that of without light. Particularly, Fe-MIL-101-2 shows the highest removal efficiency of 100% within 120 min under the visible-light irradiation, which was 1.8 times higher than that of without light (Fig. 3(b)). The suitable molar ratio content of H_2BDC and H_2BDC-NH_2 in the Fe-MIL-101 frameworks can enhance charge separation at the interface, resulting in the highly photocatalytic reduction of Cr(VI). As expected, the pseudo-first-order kinetic constant value (k) of Fe-MIL-101-2 (0.028 $g{\cdot}mg^{-1}{\cdot}min^{-1}$) is also highest among all samples under the visible-light irradiation (Table S7 in the ESM), further indicating its reinforced performance. This value is superior to many of the reported photocatalysts (Table S8 in the ESM).

The above outstanding results suggest the capability of Fe-MIL-101-2 for Cr(VI) photocatalytic reduction and adsorption motivated us to investigate the adsorption isotherms (Fig. 3(c)). Remarkably, the Fe-MIL-101 series exhibited enhanced Cr(VI) uptake at higher initial concentrations, with the adsorption data being well described by the Langmuir mode (Fig. S26 in the ESM). Under the visible-light irradiation, the slightly concave octahedron Fe-MIL-101 exhibits the lowest maximum adsorption capacity of 132.48 $mg{\cdot}g^{-1}$ (Table S11 in the ESM). By introducing the function group of $-NH_2$ into the Fe-MIL-101 an enhanced adsorption capacity (181.16 $mg{\cdot}g^{-1}$) of solid octahedron Fe-MIL-101-NH_2 can be observed, which can be attributed to the improved light absorption and mass transfer. Furthermore, accounting to the advantages of rich mesopores of star-concave structure, Fe-MIL-101-2 shows the highest Cr(VI) adsorption capacity with a maximum uptake of 238.82 $mg{\cdot}g^{-1}$. Such a significantly boosted adsorption performance can be ascribed to the structural superiorities for promoting active site exposure and electron-hole separation. However, the uptake capacities of Cr(VI) are obviously reduced to 73.88, 84.63 and 149.97 $mg{\cdot}g^{-1}$ by Fe-MIL-101, Fe-MIL-101-NH_2, and Fe-MIL-101-2 without light, respectively (Fig. 3(d)). Therefore, it can be concluded that light plays an important synergistic role in the Cr(VI) removal process. In addition, the introduction of hole scavenger into the Cr(VI) photoreduction system can further improve the removal efficiency of Cr(VI) (Fig. 3(c)). Notably, the maximum adsorption capacity of Cr(VI) can reach to 268.88 $mg{\cdot}g^{-1}$ for the star-concave Fe-MIL-101-2 with the introduction of oxalic acid (Oxa) (Table S11 in the ESM). This intensified photocatalytic activity of Fe-MIL-101-2 can be observed due to the effective capture of photoinduced holes by Oxa, resulting in high separation and accumulation of electrons for Cr(VI) reduction.

As the competing ions in wastewater can also interfere with the efficiency of Cr(VI), we therefore conducted the selective removal of Cr(VI) experiment by Fe-MIL-101-2 in the presence of various coexisting anions (Fig. 3(e)). Interestingly, when the concentration of Cr(VI) and competing ions is 10 ppm, the removal efficiency of Cr(VI) by Fe-MIL-101-2 showed negligible effect with all the competitive anions. Moreover, when the concentration of competing ions increased to 50 ppm, only HPO_4^{2-} and CO_3^{2-} had slightly hindered the removal of Cr(VI). Given the excellent selective uptake of Cr(VI), we further investigated the stability of Fe-MIL-101-2 on the basis of multiple cycles for photoreduction of Cr(VI). Intriguingly, Fe-MIL-101-2 showed excellent cycling performance with slight decrease in the Cr(VI) removal efficiency after eight cycles (Fig. 3(f)). Moreover, PXRD pattern of the star-concave Fe-MIL-101-2 after the eight times reuse shows no obvious changes as compared with used before (Fig. S27 in the ESM). The SEM and TEM images of the Fe-MIL-101-2 after adsorption-photoreduction of Cr(VI) show no significant changes in star-concave morphology (Fig. S28 in the ESM).

To probe the optical properties of the as-synthesized samples, the ultraviolet–visible (UV–vis) diffuse reflectance spectra (DRS) were firstly performed. As shown in Fig. 4(a), the absorption edges of Fe-MIL-101 and Fe-MIL-101-NH_2 were located at 430 and 600 nm, respectively. As compared with Fe-MIL-101, the absorption edge of Fe-MIL-101-NH_2 undergoes an obvious redshift, due to that the amine functional group can ensure rich conjugated π electrons to Fe-oxo centers [32]. The Fe-MIL-101-x with the different amounts of amine group has similar absorption edges to that of Fe-MIL-101-NH_2. Compared with Fe-MIL-101, all Fe-MIL-101-x samples exhibit enhanced absorbance in the visible-light region. Correspondingly, Fe-MIL-101-2 shows the strongest optical response among them in the region of visible-light, indicating that optimizing the molar ratio of H_2BDC and NH_2-BDC in the Fe-MIL-101-x frameworks is of vital importance to obtain maximum light absorption. Based on the Tauc plots, the bandgaps (E_g) of Fe-MIL-101, Fe-MIL-101-NH_2, Fe-MIL-101-0.25, Fe-MIL-101-0.5, Fe-MIL-101-1, Fe-MIL-101-2, and Fe-MIL-101-4 were determined to be 2.98, 2.86, 2.79, 2.72, 2.70, 2.67, and 2.84 eV, respectively (Fig. 4(b)). These results demonstrate that the introduction of mixed ligands to form Fe-MIL-101-x can reduce the bandgap of Fe-MIL-101 framework which is due to the enhancement of conjugation between the amine group and Fe-oxo centers via π electrons transfer. Further, the positive slopes of the Mott–Schottky plots indicate that Fe-MIL-101, Fe-MIL-101-NH_2, and Fe-MIL-101-2 are n-type semiconductors (Fig. 4(c)). The flat band potentials (equal to conduction band (CB)) of Fe-MIL-101, Fe-MIL-101-NH_2 and Fe-MIL-101-2 were fitted to be −0.53, −0.56, and −0.62 eV vs. Ag/AgCl (−0.33, −0.36, −0.42 eV vs. normal hydrogen electrode (NHE)), respectively. Consequently, the valence band (VB) potentials of Fe-MIL-101, Fe-MIL-101-NH_2, and Fe-MIL-101-2 were calculated to be 2.65, 2.5, and 2.25 eV vs. NHE, respectively. The CB of all the frameworks is more negative than the redox potential of Cr(VI)/Cr(III) (0.51 eV) [33]. Therefore, all of the Fe-MIL-101, Fe-MIL-101-NH_2, and Fe-MIL-101-2 are thermodynamically suitable for photoreduction of Cr(VI) via photoinduced electrons.

To further reveal the advantages of Fe-MIL-101-2, transient photocurrent measurements, electrochemical impedance spectroscopy (EIS), and PL spectra were performed. As shown in Fig. 4(d), Fe-MIL-101-2 exhibited the highest photocurrent density than Fe-MIL-101 and Fe-MIL-101-NH_2 within the visible light irradiation on-off cycles. Such results prove that Fe-MIL-101-2 has the highest charge separation and transfer efficiency among the three samples. Meanwhile, the EIS results are presented in Fig. 4(e). It is well known that the higher radius of EIS arc in Nyquist plots corresponds to the higher charge-transfer resistance (R_{ct}) of photocatalyst. Notably, Fe-MIL-101-2 shows the smallest arc radius, suggesting that it has the minimal interfacial R_{ct} of photo-excited carriers. Additionally, the results are also confirmed by PL spectra (Fig. 4(f)). As compared the PL spectra with the three samples, we can see that Fe-MIL-101-NH_2 presented much weaker intensity than Fe-MIL-101, suggesting the amine functional group is beneficial for the photogenerated electrons-holes separation [34]. Interestingly, the weakest PL intensity of Fe-MIL-101-2 can be seen

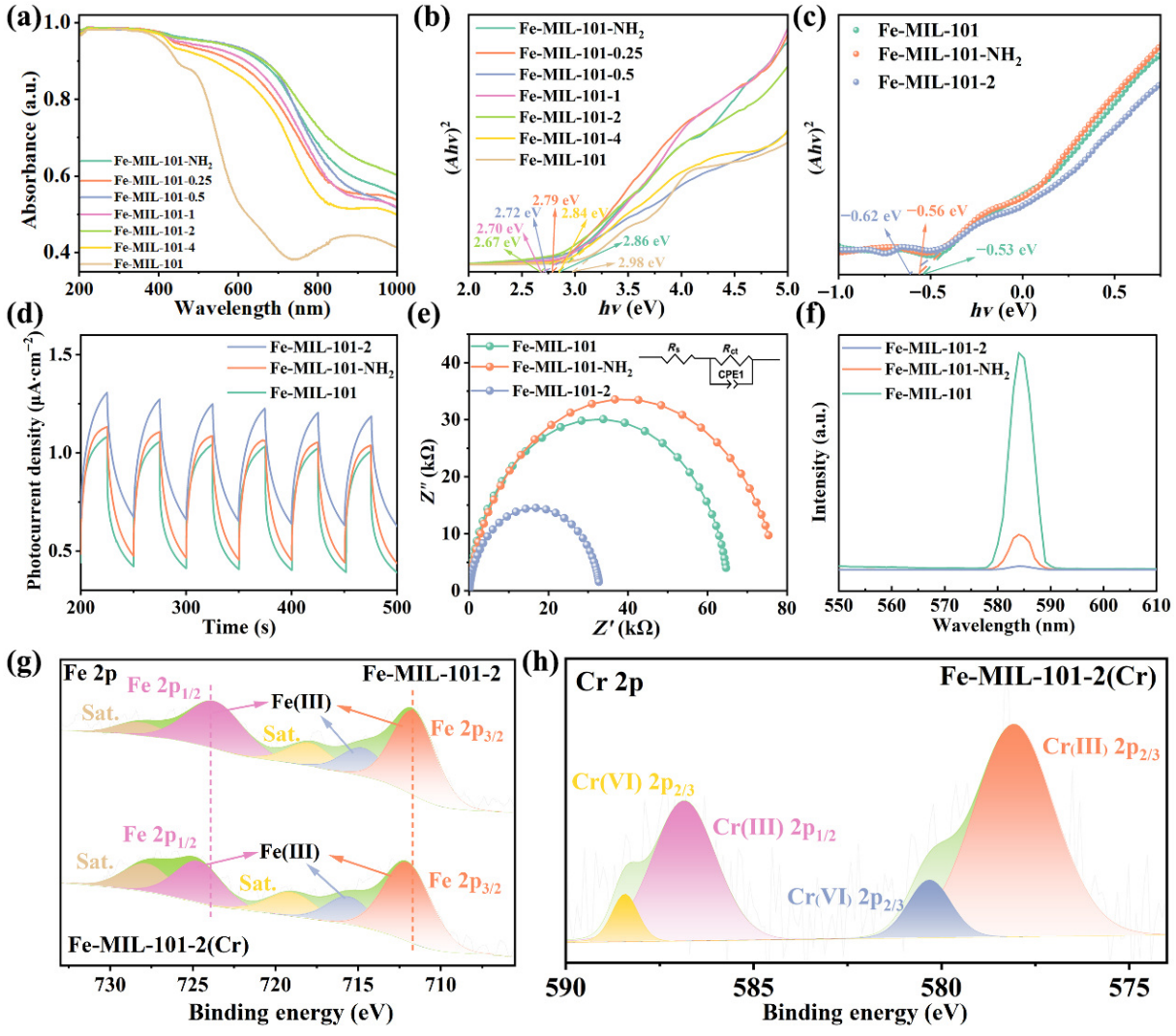

Figure 4 Optoelectronic properties of Fe-MIL-101, Fe-MIL-101-NH_2, and Fe-MIL-101-2. UV–Vis DRS spectra (a), Tauc plot curves (b), Mott–Schottky plots (c), transient photocurrent responses (d), and Nyquist impedance plots (e). (f) PL spectra of Fe-MIL-101, Fe-MIL-101-NH_2, and Fe-MIL-101-2. High-resolution XPS spectra of Fe 2p for Fe-MIL-101-2 and Fe-MIL-101-2(Cr) (g) and Cr 2p for Fe-MIL-101-2(Cr) (h).

in Fig. 4(f), demonstrating the highest photogenerated electron-holes separation efficiency over Fe-MIL-101-2, thus leading to enhanced photocatalytic activity. To understand the mechanism of photo enhanced enrichment of Cr(VI), the XPS spectra of Fe-MIL-101-2 before and after adsorption (Fe-MIL-101-2(Cr)) were performed. For Fe-MIL-101-2, peaks at 711.6 and 723.8 eV can be assigned to the the Fe $2p_{3/2}$ and Fe $2p_{1/2}$ of Fe^{3+} (Fig. 4(g)) [35]. Whereas for Fe-MIL-101-2(Cr), the Fe^{3+} 2p (712.5 eV for Fe $2p_{3/2}$ and 724.7 eV for Fe $2p_{1/2}$) after adsorption under visible-light irradiation becomes slightly higher as compared to Fe-MIL-101-2 before adsorption, demonstrating that the Fe^{3+} active center of framework plays a key role for the Cr(VI) removal. While, in Fe-MIL-101-2 (Cr), there are two Cr(III) peaks of 577.2 and 586.9 eV besides the peaks for Cr(VI) [21], indicating that Cr(VI) can be photocatalytically reduced to Cr(III) by Fe-MIL-101-2 under visible-light irradiation (Fig. 4(h)).

The electronic structure and local coordination environment of MIL-Fe-101-2 before and after adsorption-photoreduction of the Cr(VI) were performed by the X-ray absorption fine structure (XAFS). The X-ray absorption near-edge structure (XANES) and extended X-ray absorption fine structure (EXAFS) analyses of Fe K-edge and Cr K-edge were investigated owing to that 3d element K-edge is sensitive to the local coordination environment [36]. The Fe K-edge XANES spectra of Fe-MIL-101-2 and Fe-MIL-101-2(Cr) with Fe foil and Fe_2O_3 as references are shown in Fig. 5(a). The Fe K-edge XANES spectra exhibited that the white line of Fe-MIL-101-2 is close to that of Fe_2O_3, indicating that the oxidation state of Fe in Fe-MIL-101-2 is Fe^{3+} [37]. Additionally, upon magnifying the absorption edge, the Fe K-edge XANES spectra of Fe-MIL-101-2(Cr) show a higher energy shift after photocatalytic reduction, due to the higher valence state of Fe caused by the photoreduction of Cr(VI) in Fe-MIL-101-2. This observation demonstrates that electronic transfer occurred during the photocatalytic reduction of Cr(VI), with electrons transferring from Fe to Cr in Fe-MIL-101-2(Cr). Further, the Fourier transformed (FT) oscillation $k^3\chi(k)$ functions of k-space for the Fe-MIL-101-2 and Fe-MIL-101-2(Cr) exhibit an obvious difference in the middle k region (7–9 Å), suggesting the distinct interactions between the Fe and Cr atoms of Fe-MIL-101-2 after photocatalytic reduction of Cr(VI) (Fig. S38 in the ESM). Subsequently, such difference of Fe-MIL-101-2 and Fe-MIL-101-2(Cr) can be more clearly seen in R-space EXAFS spectra (Fig. 5(b)). As can be seen in Fig. 5(b), Fe-MIL-101-2 has a strong

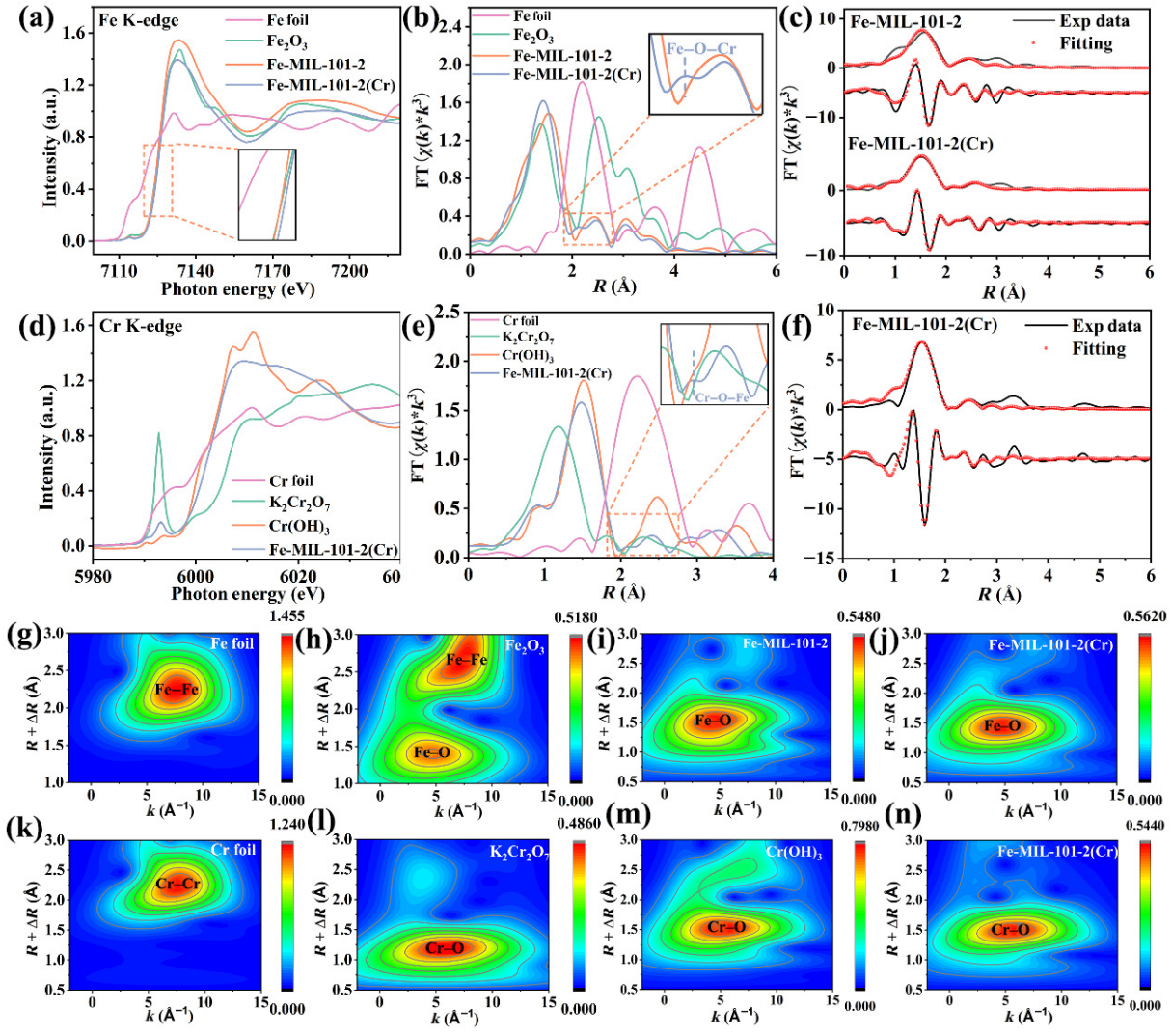

Figure 5 Fe K-edge XANES spectra (a) and the corresponding FT-EXAFS spectra in *R* space (b) of Fe foil, Fe_2O_3, Fe-MIL-101-2, and Fe-MIL-101-2(Cr). The Fe K-edge EXAFS fitting curves of Fe-MIL-101-2 and Fe-MIL-101-2(Cr) (c), Cr K-edge XANES spectra (d), and the corresponding FT-EXAFS spectra in *R* space (e) of Cr foil, $K_2Cr_2O_7$, $Cr(OH)_3$ and Fe-MIL-101-2(Cr). (f) The Cr K-edge EXAFS fitting curves of Fe-MIL-101-2(Cr). Wavelet transform of the Fe ((g)–(j)) and Cr ((k)–(n)) K-edge of corresponding EXAFS spectra for Fe foil, Fe_2O_3, Fe-MIL-101-2, Cr foil, $K_2Cr_2O_7$, $Cr(OH)_3$, and Fe-MIL-101-2(Cr).

noticeable peak at 1.5Å belonging to the Fe–O coordination bond, while no distinct Fe–Fe bond (2.2 Å) can be seen. Significantly, Fe–O bond length of Fe-MIL-101-2(Cr) (1.4 Å) after photocatalytic reaction is negatively shifted by 0.1 Å as compared with that of Fe-MIL-101-2, which indicates that the adsorption-photoreduction of the Cr(VI) can influence the electronic structure of the framework through Fe–O–Cr bonds. Meanwhile, it is noteworthy that a new formation of Fe–O–Cr bond (2.1 Å) can be seen in Fe-MIL-101-2(Cr). This indicates that the Cr(VI) is immobilized by sharing O atoms from $Cr_2O_7^{2-}$ with Fe-MIL-101-2 to form new Fe–O–Cr coordination bonds. Further, the coordination configuration around the Fe before and after adsorption-photoreduction of the Cr(VI) of MIL-Fe-101-2 was analyzed by fitting the k^3-weighted EXAFS data in *R*-space (Fig. 5(c)). The fitting results are summarized in Table S12 in the ESM. As seen, the first shell of MIL-Fe-101-2 is attributed to Fe–O distance of 2.04 Å and a coordination number of 5.3, while the second shell corresponds to the Fe–C at distance 3.1 Å with a coordination number of 3.6. However, for Fe-MIL-101-2(Cr), the first Fe–O shell has a bond distance of 1.96 Å and a coordination number of 4.5, whereas the second shell represents the Fe–O–Cr bond at 2.22 Å with a coordination number of 0.9. Additionally, the third shell corresponds to the Fe–C at distance of 2.91 Å with a coordination number of 2.7. Such EXAFS fitting results showed that the bond lengths and coordination numbers of Fe–O and Fe–C in Fe-MIL-101-2(Cr) were slightly reduced as compared to those of Fe-MIL-101-2, further confirming the formation of Fe–O–Cr bond.

On the other hand, the local coordination environments of Cr adsorbed in Fe-MIL-101-2(Cr) along with the references Cr foil, $K_2Cr_2O_7$ and $Cr(OH)_3$ were also investigated by XAFS. From Fig. 5(d), the Cr K-edge XANES spectra exhibited that the absorption edge of Fe-MIL-101-2(Cr) is close to that of $Cr(OH)_3$, suggesting that the oxidation state of Cr in Fe-MIL-101-2(Cr) is Cr(III) [38]. This suggests that there is a photoreduction occurring during such adsorption process. Further, the corresponding FT-EXAFS spectra of Fe-MIL-101-2(Cr) and the references are shown in Fig. 5(e). The dominant peak at 1.51 Å belonging to Cr–O coordination bond, while a new peak at 2.12 Å corresponding to Cr–O–Fe bond can be only observed in Fe-MIL-101-2(Cr), which is consistent with that of Fe FT-EXAFS spectra (Fig. 5(b)). The

EXAFS fitting results exhibited that the first shell of Fe-MIL-101-2(Cr) is attributed to Cr–O at a distance of 1.98 Å with a coordination number of 2.7, while the second Cr–O shell with a distance at 2.75 Å and coordination number of 0.9. These results showed that the second Cr–O length is much longer than that of the first Cr–O bond of Cr(III), which suggests that the O atom at second Cr–O shell of Fe-MIL-101-2(Cr) is from Fe-MIL-101-2 rather than Cr(III). Therefore, it can be concluded that the Cr(III) is fixed by sharing O atom of Fe-MIL-101-2 while forming Cr–O–Fe bond. Additionally, the EXAFS wavelet transforms (WT) were conducted to confirm the Fe (Figs. 5(g)–5(j)) and Cr (Figs. 5(k)–5(n)) atoms coordination situation in Fe-MIL-101-2 before and after the adsorption-photoreduction of the Cr(VI). Fe-MIL-101-2 shows the WT contour plot intensity maximum at 4.8 $Å^{-1}$ for Fe–O bond, which is similar to that of the Fe_2O_3. However, the Fe K-edge WT contour plot intensity maximum with Fe–O bond of Fe-MIL-101-2(Cr) is 5.0 $Å^{-1}$, which is a little shifted upwards compared to Fe-MIL-101-2. Meanwhile, the Cr K-edge WT contour plot in the Fe-MIL-101-2(Cr) presents the intensity maximum color with Cr–O bond at 5.3 $Å^{-1}$, which is similar to that of the $Cr(OH)_3$. These combined results confirm that the adsorption-photoreduction process can modulate the local electronic structure of the Fe K-edge in Fe-MIL-101-2, resulting in significant enhancement of photocatalytic performances.

To gain insights into the mechanism of adsorption-photoreduction of Cr(VI), the DFT calculations were conducted (Fig. 6). Utilizing MOFs for photocatalytic reduction of Cr(VI) is an efficient and environmentally friendly strategy. However, to optimize the performance of MOF materials, it is crucial to deeply understand the relationship between their electronic structure and catalytic mechanisms. According to previous studies, the crystalline structure of MIL-101 was used as the experimental based model and Fe-MIL-101, Fe-MIL-101-NH_2 and Fe-MIL-101-2 were designed accordingly. Through quantum chemical optimization, the electronic transition properties between the highest occupied molecular orbital (HOMO) and the lowest unoccupied molecular orbital (LUMO) were investigated, along with their impact on photocatalytic activity. The HOMO–LUMO energy gap (*E*) is a crucial indicator of the photocatalytic performance of materials [39, 40]. Results showed that Fe-MIL-101-2 exhibited the smallest HOMO–LUMO energy gap, indicating greater sensitivity to photoexcitation and easier generation of photogenerated electrons and holes, which favors the reduction of Cr(VI). The electron cloud distributions of HOMO and LUMO also reflect the electronic transition pathways of the materials. HOMO is primarily localized on the π orbitals of the ligands, while LUMO is concentrated on the d orbitals of the metal clusters. This distribution facilitates efficient electron transfer between the ligands and the metal clusters. In electronic structure calculations, the HOMO (Figs. 6(a), 6(e), and 6(i)) and LUMO (Figs. 6(b), 6(f), and 6(j)) characteristics of Fe-MIL-101, Fe-MIL-101-NH_2, and Fe-MIL-101-2 with band structure diagrams visually demonstrate the regulatory effects of different modifications on the electronic structure of the materials. Further, the charge density distributions show that the central iron atom charges for Fe-MIL-101 (Fig. 6(c)), Fe-MIL-101-NH_2 (Fig. 6(g)), and Fe-MIL-101-2 (Fig. 6(k)) are 0.871, 0.881, and 0.925, respectively. This indicates that the electron donation ability of different ligands significantly affects the electronic environment of the central Fe cluster. Carboxyl and amino ligands enhance the surrounding negative charge through p-π conjugation with the benzene ring, resulting in higher positive charges on the central Fe cluster. For Fe-MIL-101-NH_2, the interaction between amino ligands weakens the stable p-π conjugation structure, leading to a relatively lower charge on the central Fe cluster. For Fe-MIL-101-2, the Fe atom has the largest charge density, indicating the favorable electron-withdrawing capability of the Fe central in frameworks for enhancing the adsorption-photoreduction of Cr(VI) performance. The molecular electrostatic potential (MESP) is an effective tool for studying the nucleophilic and electrophilic activity of MOFs. Figures 6(d), 6(h), and 6(l) show that the primary adsorption active sites are near the Fe metal central and the amino and carboxyl groups of the ligands. Significantly, the active sites show more concentrated electrostatic potential distribution in Fe-MIL-101-2, making it as the strongest adsorption of Cr(VI). Furthermore, the projected partial density of state (PDOS) was performed to investigate the electronic structures of Fe-MIL-101, Fe-MIL-101-NH_2, and Fe-MIL-101-2 (Fig. 6(m)). In the region of −6 to −4 eV, Fe-MIL-101-2 exhibits a high peak, particularly with the curve of Fe (−8 to −6 eV) showing significant electronic state density, indicating that the d-orbitals of Fe play a crucial role in the low-energy states. The contributions of C and O are distributed between −4 and 0 eV, reflecting the important role of the organic ligand in the Fe-MIL-101-2 near the Fermi level. In the region of 0 to 2 eV, the electronic state density is relatively low but more concentrated, which is consistent with Fe-MIL-101-2 having the narrow bandgap. As compared to Fe-MIL-101 and Fe-MIL-101-NH_2, Fe-MIL-101-2 shows the narrowest band gap near the Fermi level, further confirming its highest electron transfer and enhances photocatalytic performance [41].

To quantitatively evaluate the adsorption performance of Fe-MIL-101, Fe-MIL-101-NH_2 and Fe-MIL-101-2 on Cr(VI), the adsorption energies were calculated (Fig. 6(n)). As seen, the adsorption energies of Fe-MIL-101, Fe-MIL-101-NH_2, and Fe-MIL-101-2 were −3.02, −4.18, and −7.25 eV, respectively, indicating that Fe-MIL-101-2 possesses the strongest adsorption capacity toward Cr(VI). These computational results are consistent with the experimental results. The combined experimental and theoretical analyses further validate the regulatory effect of mixed ligand modifications on the electronic structure and photocatalytic performance of Fe-MIL-101.

All these results indicate that the star-concave Fe-MIL-101-2 shows the outstanding performance for the adsorption-photoreduction of Cr(VI). Based on the above experimental and theoretical calculation results, a plausible Cr(VI) adsorption-photoreduction removal mechanism by Fe-MIL-101-2 is shown in Fig. 6(o) [32, 42]. In the structure of the star-concave Fe-MIL-101-2, the Fe–O clusters act as quantum dots, while the H_2BDC-NH_2 ligand and the star-concave structure serve as a visible light absorption center. Firstly, under the visible light irradiation, H_2BDC-NH_2 ligand and the star-concave structure in Fe-MIL-101-2 powerfully absorbed and enriched the visible light. Then the photogenerated electrons have been efficiently transferred to the Fe–O clusters of LUMO potential in the frameworks via ligand-to-metal charge transfer, leaving behind holes in the HOMO potential of Fe-MIL-101-2. Finally, the photogenerated electrons in the LUMO potential are accepted by Cr(VI) which adsorbed on Fe–O clusters. Meanwhile, the holes in the HOMO potential oxidize the hole scavenger of Oxa which adsorbed on the –NH_2 group. Thus, the adsorption and photocatalysis of the star-concave Fe-MIL-101-2 synergistically work together to efficiently realize the removal of Cr(VI).

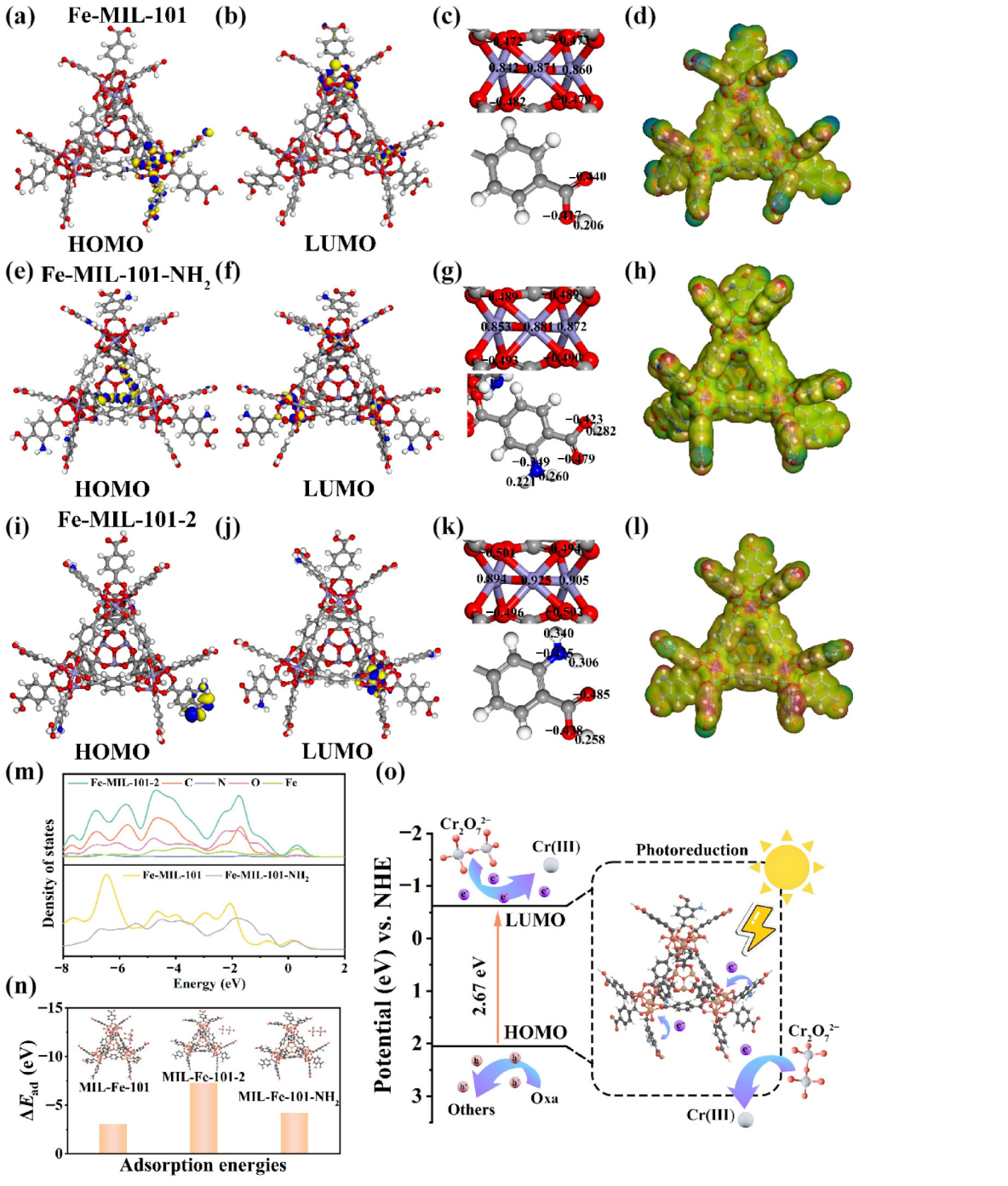

Figure 6 The HOMO ((a), (e), and (i)) and LUMO ((b), (f), and (j)) orbital distributions, charge density differences ((c), (g), and (k)), MESP distributions ((d), (h), and (l)), PDOS (m) and adsorption energies of Cr(VI) (n) over Fe-MIL-101, Fe-MIL-101-NH_2, and Fe-MIL-101-2. (o) Proposed mechanism of photoreduction of Cr(VI) over Fe-MIL-101-2.

3 Conclusions

In summary, we successfully prepared a novel star-concave MOFs with high specific surface area and rich hierarchical pores, namely Fe-MIL-101-2, through a facile linker competitive coordination induced interface assembly strategy. The key route of the star-concave structure MOFs is attributed to the competition between the two electronegativity difference linkers for the kinetics nucleation and oriented growth to form star-concave structure by judicious adjusting the deposition and diffusion rates of unit. The star-concave Fe-MIL-101-2 featured good visible-light trapping, narrow bandgap and preferred charge transfer, resulting in an excellent photoreduction activity of Cr(VI), coupled with high capacity, rapid kinetics and long recyclability under visible-light irradiation. In addition, by combing the experiments, EXAFS, FEM and DFT calculations, the synergistic adsorption-photoreduction removal of Cr(VI) mechanism by star-concave Fe-MIL-101-2 has been comprehensively investigated. This present research provides a new strategy for the rational construction of efficient MOFs photocatalysts for environmental water remediation.

Electronic Supplementary Material: Supplementary material (experimental section and experimental data including TGA curves, FTIR spectra, SEM images, TEM images, EDX, PXRD patterns, BET surface areas, pore volumes, XPS spectra, EXAFS spectra, adsorption and photocatalytic reduction of Cr(VI) performance) is available in the online version of this article at https://doi.org/10.26599/NR.2025.94908052.

Data availability

All data needed to support the conclusions in the paper are presented in the manuscript and the Electronic Supplementary Material. Additional data related to this paper may be requested from the corresponding author upon request.

Acknowledgements

This work was supported by the National Natural Science Foundation of China (No. 21501003) and the Open Fund of Anhui Institute of Urban-Rural Green Development and Urban Renewal (No. 2304001). We thank Dr. Leijie Zhang (Specreation Instruments Co., Ltd.) for his assistance for XAFS characterization and related data analysis.

Declaration of competing interest

All the contributing authors report no conflict of interests in this work.

Author contribution statement

Y. R. C. and Y. Q. G.: Designed the experiments, data curation, writing – original draft. Y. P.: Investigation, conceptualization. Y. J. Z.: DFT calculation. K. F. and C. G. P.: Formal analysis, methodology. J. Q. L., A. K., H. P., and F. K.: Supervision, funding acquisition, writing – review & editing. All authors discussed the results and commented on the paper.

Use of AI statement

None.

References

[1] Lim, H.; Kwon, H.; Kang, H.; Jang, J. E.; Kwon, H. J. Semiconducting MOFs on ultraviolet laser-induced graphene with a hierarchical pore architecture for NO_2 monitoring. *Nat. Commun.* **2023**, *14*, 3114.

[2] Luo, S. Y.; Liu, Z. Z.; Yin, X. R.; Lin, Z. P.; Zhang, S.; Chen, J. F.; Guo, M. H. A sandwich structure Ag/$MgFe_2O_4$-deposited surface carbonized wood for integrated solar steam generation and photoreduction of Cr(VI). *Small* **2024**, *20*, 2309087.

[3] Kaur, H.; Chandel, S. S.; Karmakar, A.; Sinha-Ray, S.; Krishnan, V.; Koner, R. R. Mercapto-decorated Zn-based metal-organic framework embedded nanofibrous membrane for oxo-anions treatment in aqueous solution. *Chem. Eng. J.* **2022**, *443*, 136212.

[4] Prakash Tripathy, S.; Subudhi, S.; Das, S.; Kumar Ghosh, M.; Das, M.; Acharya, R.; Acharya, R.; Parida, K. Hydrolytically stable citrate capped Fe_3O_4@UiO-66-NH_2 MOF: A hetero-structure composite with enhanced activity towards Cr(VI) adsorption and photocatalytic H_2 evolution. *J. Colloid Interface Sci.* **2022**, *606*, 353–366.

[5] Ji, W.; Wang, X. B.; Ding, T. Q.; Chakir, S.; Xu, Y. F.; Huang, X. H.; Wang, H. T. Electrospinning preparation of nylon-6@UiO-66-NH_2 fiber membrane for selective adsorption enhanced photocatalysis reduction of Cr(VI) in water. *Chem. Eng. J.* **2023**, *451*, 138973.

[6] Hu, Y.; Jin, Y. Z.; Gao, Y. Q.; Li, M. F.; Wang, X. J.; Ma, H. Y.; Zhang, Y. N. Interface and defect engineering in 3D $Co_3O_{4\text{-}Ov}$/TiO_2 to boost simultaneous removal of BPA and Cr(VI) upon photoelectrocatalytic/peroxymonosulfate (PEC/PMS) system. *Adv. Funct. Mater.* **2025**, *35*, 2414350.

[7] Zhu, T. T.; Yao, Z. F.; Pan, J. H.; Hu, F. T.; Zhang, S. M.; Fan, S. Y.; Xing, C. C.; Yu, Z. B.; Wang, S. F.; Hou, Y. P. Biomass-derived carbon quantum dots chemical bonding with Sn-doped $Bi_2O_2CO_3$ endowed fast carriers' dynamics and stabilized oxygen vacancies for efficient decontamination of combined pollutants. *Small* **2024**, *20*, 2311916.

[8] Zhao, W.; Li, J.; She, T. T.; Ma, S. S.; Cheng, Z. P.; Wang, G. X.; Zhao, P. S.; Wei, W.; Xia, D. H.; Leung, D. Y. C. Study on the photocatalysis mechanism of the Z-scheme cobalt oxide nanocubes/carbon nitride nanosheets heterojunction photocatalyst with high photocatalytic performances. *J. Hazard. Mater.* **2021**, *402*, 123839.

[9] Xu, B.; Wang, X. B.; Huang, Y. Y.; Liu, J.; Wang, D.; Feng, S. J.; Huang, X. H.; Wang, H. T. Electrospinning preparation of PAN/TiO_2/PANI hybrid fiber membrane with highly selective adsorption and photocatalytic regeneration properties. *Chem. Eng. J.* **2020**, *399*, 125749.

[10] Zhang, S.; Chen, L. X.; Qu, Z. Y.; Zhai, F. W.; Yin, X. X.; Zhang, D.; Shen, Y. F.; Li, H.; Liu, W.; Mei, S. et al. Confining Ti-oxo clusters in covalent organic framework micropores for photocatalytic reduction of the dominant uranium species in seawater. *Chem* **2023**, *9*, 3172–3184.

[11] Naghdi, S.; Brown, E.; Zendehbad, M.; Duong, A.; Ipsmiller, W.; Biswas, S.; Toroker, M. C.; Kazemian, H.; Eder, D. Glyphosate adsorption from water using hierarchically porous metal-organic frameworks. *Adv. Funct. Mater.* **2023**, *33*, 2213862.

[12] Tang, Y. Y.; Luo, X.; Xia, R. Q.; Luo, J.; Peng, S. K.; Liu, Z. N.; Gao, Q.; Xie, M.; Wei, R. J.; Ning, G. H. et al. Molecular engineering of metal-organic frameworks for boosting photocatalytic hydrogen peroxide production. *Angew. Chem., Int. Ed.* **2024**, *63*, e202408186.

[13] Sun, K.; Huang, Y.; Sun, F. S.; Wang, Q. Y.; Zhou, Y. J.; Wang, J. X.; Zhang, Q.; Zheng, X. S.; Fan, F. T.; Luo, Y. et al. Dynamic structural twist in metal-organic frameworks enhances solar overall water splitting. *Nat. Chem.* **2024**, *16*, 1638–1646.

[14] Liang, R. R.; Yang, Y. H.; Han, Z. S.; Bakhmutov, V. I.; Rushlow, J.; Fu, Y. B.; Wang, K. Y.; Zhou, H. C. Zirconium-based metal-organic frameworks with free hydroxy groups for enhanced perfluorooctanoic acid uptake in water. *Adv. Mater.* **2024**, *36*, 2407194.

[15] Liu, H. D.; Cheng, M.; Liu, Y.; Zhang, G. X.; Li, L.; Du, L.; Li, B.; Xiao, S.; Wang, G. F.; Yang, X. F. Modified UiO-66 as photocatalysts for boosting the carbon-neutral energy cycle and solving environmental remediation issues. *Coord. Chem. Rev.* **2022**, *458*, 214428.

[16] Wang, X. S.; Chen, C. H.; Ichihara, F.; Oshikiri, M.; Liang, J.; Li, L.; Li, Y. X.; Song, H.; Wang, S. Y.; Zhang, T. et al. Integration of adsorption and photosensitivity capabilities into a cationic multivariate metal-organic framework for enhanced visible-light photoreduction reaction. *Appl. Catal. B: Environ.* **2019**, *253*, 323–330.

[17] Zhou, X. Y.; Wang, T. Y.; He, D.; Chen, P.; Liu, H.; Lv, H. Y.; Wu, H. N.; Su, D. W.; Pang, H.; Wang, C. Y. Efficient photocatalytic desulfurization in air through improved photogenerated carriers separation in MOF MIL101/carbon dots-g-C_3N_4 nanocomposites. *Angew. Chem., Int. Ed.* **2024**, *63*, e202408989.

[18] Li, S. J.; Wang, C. C.; Dong, K. X.; Zhang, P.; Chen, X. B.; Li, X. MIL-101(Fe)/BiOBr S-scheme photocatalyst for promoting photocatalytic abatement of Cr(VI) and enrofloxacin antibiotic: Performance and mechanism. *Chin. J. Catal.* **2023**, *51*, 101–112.

[19] Lu, W.; Wang, C.; Song, W. H.; Zhang, Z. X.; Xie, C. D.; Wang, J. J. High-efficiency photocatalytic reduction of Cr(VI) by Z-scheme

electron transfer in UiO-66-NH_2@HDU-25 heterojunctions. *J. Mater. Chem. A* **2024**, *12*, 20149–20159.

[20] Li, S. J.; Wang, C. C.; Liu, Y. P.; Liu, Y. Z.; Cai, M. J.; Zhao, W.; Duan, X. G. S-scheme MIL-101(Fe) octahedrons modified Bi_2WO_6 microspheres for photocatalytic decontamination of Cr(VI) and tetracycline hydrochloride: Synergistic insights, reaction pathways, and toxicity analysis. *Chem. Eng. J.* **2023**, *455*, 140943.

[21] Song, X. L.; Dai, R. W.; Zhu, T.; Zhang, S. W.; Liu, J. L.; Zhang, S. L.; Zhang, L. F. A novel iron metal organic framework-based nanocomposite for the synergistic degradation and adsorption of organic pollutants and Cr(VI) under visible light. *J. Clean. Prod.* **2024**, *456*, 142337.

[22] Geng, P. B.; Wang, L.; Du, M.; Bai, Y.; Li, W. T.; Liu, Y. F.; Chen, S. Q.; Braunstein, P.; Xu, Q.; Pang, H. MIL-96-Al for Li-S batteries: Shape or size. *Adv. Mater.* **2022**, *34*, 2107836.

[23] Wu, T. Y.; Chen, G. R.; Han, J.; Sun, R. G.; Zhao, B.; Zhong, G. Y.; Yamauchi, Y.; Guan, B. Y. Construction of three-dimensional dendritic hierarchically porous metal-organic framework nanoarchitectures via noncentrosymmetric pore-induced anisotropic assembly. *J. Am. Chem. Soc.* **2023**, *145*, 16489–16507.

[24] Li, M. H.; Wang, J.; Zheng, Y. Q.; Zheng, Z. J.; Li, C. X.; Li, Z. Q. Anchoring $NaYF_4$:Yb, Tm upconversion nanocrystals on concave MIL-53(Fe) octahedra for NIR-light enhanced photocatalysis. *Inorg. Chem. Front.* **2017**, *4*, 1757–1764.

[25] Iqbal, M.; Bando, Y.; Sun, Z. Q.; Wu, K. C. W.; Rowan, A. E.; Na, J.; Guan, B. Y.; Yamauchi, Y. In search of excellence: Convex versus concave noble metal nanostructures for electrocatalytic applications. *Adv. Mater.* **2021**, *33*, 2004554.

[26] Wan, J. L.; Sun, L. C.; Sun, X. H.; Liu, C.; Yang, G. Z.; Zhang, B. B.; Tao, Y. L.; Yang, Y. H.; Zhang, Q. F. Cu^{2+} -dominated chirality transfer from chiral molecules to concave chiral Au nanoparticles. *J. Am. Chem. Soc.* **2024**, *146*, 10640–10654.

[27] Pei, C. C.; Wang, Y.; Ding, Y. J.; Li, R. X.; Shu, W. K.; Zeng, Y.; Yin, X.; Wan, J. J. Designed concave octahedron heterostructures decode distinct metabolic patterns of epithelial ovarian tumors. *Adv. Mater.* **2023**, *35*, 2209083.

[28] Wang, J.; Yuan, L.; Zhang, C. Q.; Li, S. M.; Wang, G. Z.; Wan, J. J.; Liu, C.; Yu, C. Z. Metal-organic frameworks derived titanium oxides via soft interface adaptive transformation. *Adv. Funct. Mater.* **2021**, *31*, 2107260.

[29] Zhang, G. X.; Li, Y.; Du, G. Y.; Lu, J. Q.; Wang, Q. J.; Wu, K.; Zhang, S. T.; Chen, H. Y.; Zhang, Y. Z.; Xue, H. G. et al. Spiral-concave prussian blue crystals with rich steps: Growth mechanism and coordination regulation. *Angew. Chem., Int. Ed.* **2025**, *64*, e202414650.

[30] Wu, W. B.; Decker, G. E.; Weaver, A. E.; Arnoff, A. I.; Bloch, E. D.; Rosenthal, J. Facile and rapid room-temperature electrosynthesis and controlled surface growth of Fe-MIL-101 and Fe-MIL-101-NH_2. *ACS Cent. Sci.* **2021**, *7*, 1427–1433.

[31] Jin, J.; Li, P.; Chun, D.; Jin, B. J.; Zhang, K.; Park, J. H. Defect dominated hierarchical Ti-metal-organic frameworks via a linker competitive coordination strategy for toluene removal. *Adv. Funct. Mater.* **2021**, *31*, 2102511.

[32] Guo, W. X.; Wang, S. F.; Hao, H. G.; Kong, X. J.; Yan, H.; Zhu, H. J.; Li, Y. W.; Zhou, H. W.; Zhong, D. C.; Dai, F. N. Introducing anthracene and amino groups into Ln-OFs for the photoreduction of Cr(VI) without additional photosensitizers or cocatalysts. *Inorg. Chem. Front.* **2023**, *10*, 2626–2635.

[33] Wang, X. N.; Zhang, Y.; Shi, Z. X.; Lu, T. T.; Wang, Q.; Li, B. Multifunctional Zr-MOF based on bisimidazole tetracarboxylic acid for pH sensing and photoreduction of Cr(VI). *ACS Appl. Mater. Interfaces* **2021**, *13*, 54217–54226.

[34] Kaur, B.; Soni, V.; Kumar, R.; Singh, P.; Selvasembian, R.; Singh, A.; Thakur, S.; Parwaz Khan, A. A.; Kaya, S.; Nguyen, L. H. et al. Recent advances in manipulating strategies of NH_2-functionalized metallic organic frameworks-based heterojunction photocatalysts for the sustainable mitigation of various pollutants. *Environ. Res.* **2024**, *259*, 119575.

[35] Qin, Y. B.; Zhang, M.; Zhang, F. H.; Ozer, S. N.; Feng, Y. J.; Sun, W. L.; Zhao, Y. M.; Xu, Z. L. Achieving ultrafast and highly selective capture of radiotoxic tellurite ions on iron-based metal-organic frameworks through coordination bond-dominated conversion. *J. Hazard. Mater.* **2024**, *468*, 133780.

[36] Li, C.; Zhang, W.; Cao, Y. Y.; Ji, J. Y.; Li, Z. C.; Han, X.; Gu, H. W.; Braunstein, P.; Lang, J. P. Interfacial electronic interactions between ultrathin NiFe-MOF nanosheets and ir nanoparticles heterojunctions leading to efficient overall water splitting. *Adv. Sci.* **2024**, *11*, 2401780.

[37] Bao, C. S.; Wang, H.; Wang, C. Y.; Zhang, X. H.; Zhao, X. L.; Dong, C. L.; Huang, Y. C.; Chen, S.; Guo, P.; She, X. L. et al. Cooperation of oxygen vacancy and Fe^{III}/Fe^{II} sites in H_2-reduced Fe-MIL-101 for enhanced fenton-like degradation of organic pollutants. *J. Hazard. Mater.* **2023**, *441*, 129922.

[38] Jiang, T.; Luan, W. L.; Turyanska, L.; Feng, Q. Cr_2O_3 nanoparticles boosting Cr-N-C for highly efficient electrocatalysis in acidic oxygen reduction reaction. *Int. J. Hydrog. Energy* **2021**, *46*, 18913–18921.

[39] Zhi, G.; Qi, X. J.; Li, Y. K.; Wang, J. F.; Wang, J. H. Efficient treatment of smelting wastewater: 3D nickel foam @MOF shatters the previous limitation, enabling high-throughput selective capture of arsenic to form non-homogeneous nuclei. *Sep. Purif. Technol.* **2024**, *328*, 124927.

[40] Qin, W.; Duan, R. N.; Chen, C. K.; Liao, H. Y.; Xiao, X. B.; Zheng, Z. M. Boundary effect of Ag/TiO_2 on catalytic H_2O splitting for H_2 production: A theoretical account. *Int. J. Hydrog. Energy* **2023**, *48*, 3838–3848.

[41] Wang, Q.; Zhang, C.; Huo, R. B.; Zheng, S. Z.; Liu, A. X.; Hui, Y. X.; Ji, Y.; Jin, Q.; Zhang, Z.; Tu, Y. S. et al. Novel Ag@NH_2-UiO-66(Zr) photocatalyst with controllable charge transfer pathways for efficient Cr(VI) remediation. *J. Environ. Manage.* **2024**, *367*, 122046.

[42] Liu, J.; Wu, J.; Wang, N. N.; Tian, F. S.; Li, J. Surface reconstruction of BiSI nanorods for superb photocatalytic Cr(VI) reduction under near-Infrared light irradiation. *Chem. Eng. J.* **2022**, *435*, 135152.